



CHALMERS
UNIVERSITY OF TECHNOLOGY

Kinetic Monte Carlo-Based Reactor Model Including Catalyst Shape Changes

Downloaded from: <https://research.chalmers.se>, 2025-07-02 14:03 UTC

Citation for the original published paper (version of record):

Yang, Y., Hellman, A., Grönbeck, H. (2025). Kinetic Monte Carlo-Based Reactor Model Including Catalyst Shape Changes. *ACS Catalysis*: 11502-11511. <http://dx.doi.org/10.1021/acscatal.5c01592>

N.B. When citing this work, cite the original published paper.

Kinetic Monte Carlo-Based Reactor Model Including Catalyst Shape Changes

Yuqi Yang,* Anders Hellman,* and Henrik Grönbeck*

Cite This: *ACS Catal.* 2025, 15, 11502–11511

Read Online

ACCESS |



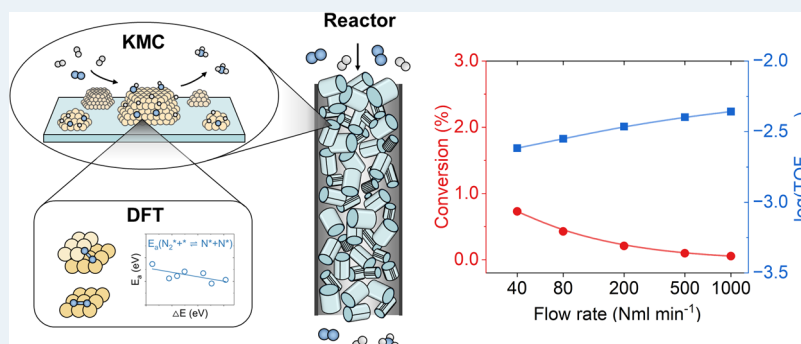
Metrics & More



Article Recommendations



Supporting Information



ABSTRACT: The dynamic character of heterogeneous catalyst particles makes direct comparisons between first-principles kinetics and experimental results obtained for technical catalysts challenging. First-principles kinetics is commonly based on a single model structure and constant reaction conditions, whereas experiments are performed over a particle distribution with shapes that respond to the reaction conditions. Here, we develop a framework for particle-shape adaptive kinetic Monte Carlo simulations in a reactor model (PAKS-R), which integrates first-principles-based kinetic Monte Carlo (kMC) simulations with a reactor model. The framework bridges the gap between the experimental situation by allowing for (i) particle size distributions, (ii) reaction conditions that change along the reactor, and (iii) dynamic shape changes of the NPs as a response to the coverages. The method is applied to ammonia synthesis over Ru NPs, reproducing the previous experimental reaction kinetics. The results show that the activity depends sensitively on the particle size and reaction conditions. The effect of dynamical shape changes is, on average, limited but strongly particle dependent. The PAKS-R approach is robust and general and can be used to explore the reaction kinetics of complex, technical catalysts for a range of reactions.

KEYWORDS: first-principles microkinetic modeling, kinetic Monte Carlo, reactor modeling, shape changes

INTRODUCTION

Technical catalysts are commonly realized as a distribution of metal nanoparticles (NPs) supported on a porous support. The NPs are typically ill-defined with respect to shape and size, which makes it challenging to unravel the contribution from the individual NPs to the overall measured catalytic activity. The situation is, furthermore, complicated by the dynamic particle shape changes, which may occur in response to variations in the reaction conditions within the reactor.^{1,2} The structural challenge has been addressed by kinetic measurements on single crystal surfaces³ or arrays of well-defined nanoparticles.^{4,5} With the model systems, it has been possible to reveal the catalytic properties of specific active sites on the NPs. However, assessing the properties of arbitrary NPs, especially under real reaction conditions, remains a significant experimental challenge.^{6,7}

Computationally, first-principles-based microkinetic simulations offer an atomistic approach to explore the role of specific sites for the activity.^{8,9} With first-principles microkinetic

simulations, it is possible to obtain information on structural dependent activity, selectivity, and dominant reaction path.^{10–12} However, direct comparisons between simulated kinetic properties and catalytic activities measured over technical catalysts are generally difficult. Current microkinetic models are often limited by: (i) The structural models are usually a small set of low-index extended surfaces; thus, models do not account for the diversity of active sites and the distribution of particle sizes and shapes that are present in technical catalysts.⁷ (ii) The applied reaction conditions in, especially, kinetic Monte Carlo (kMC) simulations, do not include the changes that occur in experimental reactors owing to the ongoing catalytic pro-

Received: March 3, 2025

Revised: May 7, 2025

Accepted: June 10, 2025

cesses.^{2,13} The reaction conditions are often fixed to the experimental operating conditions at the reactor inlet. (iii) The catalysts in simulations are typically assumed to have fixed shapes, which neglects the possibility for dynamic NP shape changes in response to the reaction conditions.^{1,14,15} With the knowledge that the measured catalytic activity depends sensitively on the particle size distribution, the particle structures, and the reaction conditions, it is essential to incorporate these effects in atomistic kinetic models.

In this work, we develop a framework for particle-shape adaptive kinetic Monte Carlo simulations in a reactor model (PAKS-R), which integrates a DFT-based kMC model with reactor simulations, Figure 1. Through iterative processes

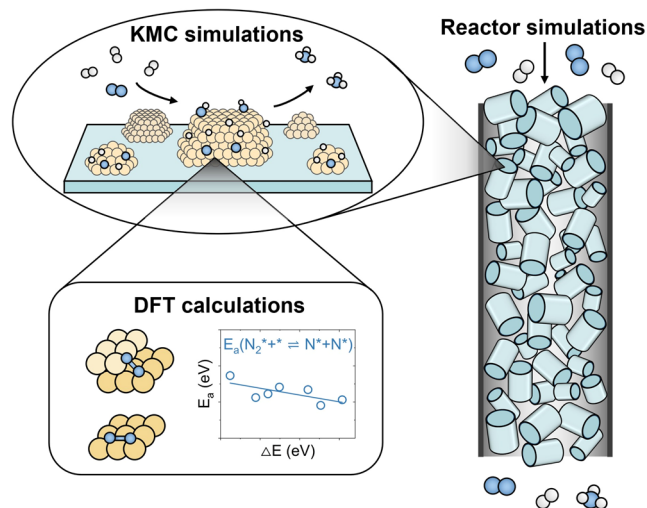


Figure 1. Schematic representation of particle-shape adaptive kinetic Monte Carlo simulations in a reactor (PAKS-R).

between the kMC and reactor simulations, PAKS-R provides a quantitative description of the averaged kinetic properties

observed over a reactor with a distribution of NPs. The Wulff shapes of the NPs are determined self-consistently as a function of the reaction conditions. By performing the kMC simulations on a distribution of NPs, PAKS-R accounts for the impact of particle size and shape distributions on the kinetic properties. Furthermore, the reactor model describes how the reaction conditions change because of the ongoing reactions and the mass transfer within the reactor.

The ammonia synthesis reaction over Ru NPs is selected as a case study to illustrate how PAKS-R describes the average kinetic properties of a reactor. Currently, the ammonia synthesis reaction consumes 1–2% of the world's total energy output and is responsible for 1% of the global carbon emissions.^{16–18} Thus, the development of more efficient and sustainable ammonia synthesis catalysts is desirable. Ru is recognized as an ideal metal catalyst for ammonia synthesis under industrial conditions,^{13,19,20} and its kinetic properties have been extensively studied.^{21–23} As the catalytic activity of ammonia synthesis is structure sensitive,^{24,25} it is important to account for the experimental size distribution of Ru NPs in kinetic simulations. In the present work, we apply PAKS-R to investigate the kinetic properties of the ammonia synthesis reaction within a reactor. The model successfully reproduces the measured conversion and TOF. By analyzing the active sites on individual NPs, we find that the kinetic properties are significantly affected by the NP size distribution and the reaction conditions. The effect on the TOF of NP-reshaping as a response to the reaction conditions is strongly dependent on the specific particle. Particle reshaping can either enhance or reduce the TOF. Thus, relying only on the computational results from a single NP may lead to an incomplete understanding regarding the effects of NP shape changes.

METHODS

Model for Particle-Shape Adaptive Kinetic Monte Carlo Simulations in a Reactor.

In the PAKS-R framework,

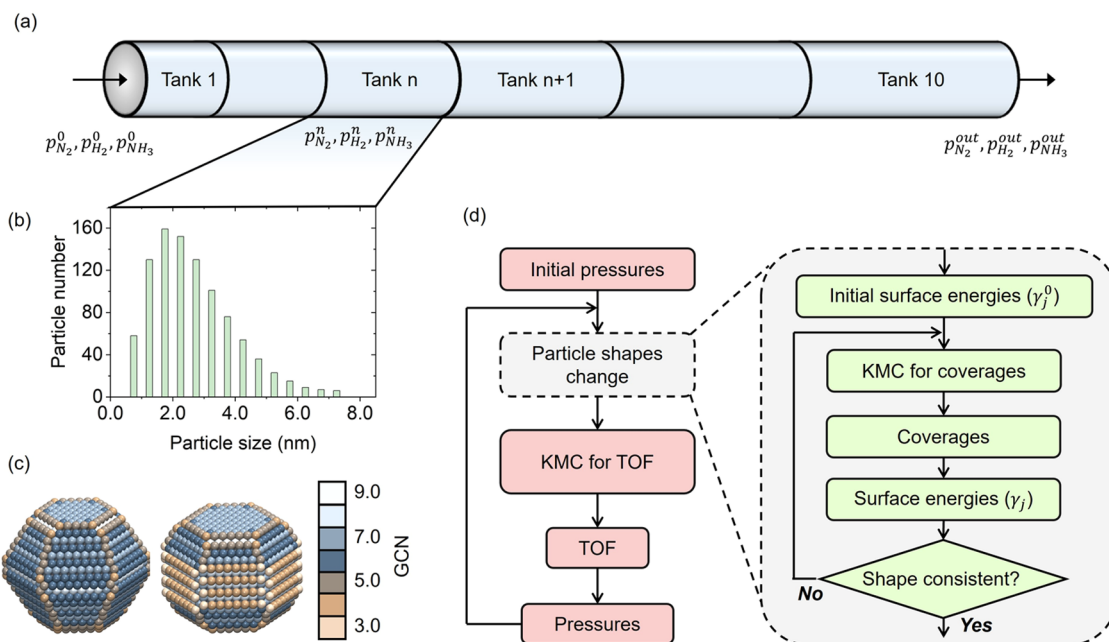


Figure 2. (a) Schematic of the plug flow reactor in PAKS-R. (b) Particle number versus particle size for the used particle distribution. (c) Wulff-constructed NPs in vacuum (left) and at reactor outlet conditions (right). (d) Flowchart of operational workflow in each tank of the plug flow reactor.

the changes in reaction conditions along the reactor are modeled using a plug flow reactor (PFR), Figure 2a. It is assumed that the catalyst material is uniformly distributed in the reactor. The PFR is, in this work, divided into 10 tanks arranged in series along the axial direction. Each tank is an ideal continuous stirred tank reactor. The reaction conditions change along the reactor, and each tank has different reaction conditions. The mass is evenly distributed in the reactor (homogeneous density throughout the reactor); however, to achieve a suitable resolution of steep gradients in partial pressures, the volume of each tank is successively increased by 50%, which effectively means that the mass that contributes to the rate is also increased by 50%.

In each tank, the particle size distribution is based on experimental data,¹⁰ Figure 2b. The simulations consider 26 types of NP in the size range from 0.88 to 7.09 nm. (See Table S1 for a description of the 26 NPs). The thermodynamic equilibrium shapes are determined by Wulff construction using the WulffPack code.²⁶ The shape of the Wulff-constructed NPs is determined by the surface energies (γ_j^0) of the Ru(0001), Ru(10 $\bar{1}$ 0), Ru(1011), Ru(10 $\bar{1}$ 2), and Ru(20 $\bar{2}$ 1) facets.²⁷ Regarding the adsorbate-induced shape changes of the NPs during reaction conditions, the surface energies γ_j of facet j are modified by the adsorption energies and surface species coverages of NH_x species, eq 1,²⁸

$$\gamma_j = \gamma_j^0 + \frac{\sum_s \theta_{s,j} \Delta E_{s,j}^{\text{ads}}}{A_{\text{site}}} \approx \gamma_j^0 + \frac{\sum_s \theta_s \Delta E_{s,j}^{\text{ads},0}}{A_{\text{site}}} \quad (1)$$

where $A_{\text{site}} = 6.15 \text{ \AA}^2$ is the surface area per atom on Ru(0001). $\theta_{s,j}$ and $\Delta E_{s,j}^{\text{ads}}$ are the coverage and adsorption energy of surface species s on facet j , respectively. $\Delta E_{s,j}^{\text{ads}}$ is approximated to be the coverage-independent adsorption energy $\Delta E_{s,j}^{\text{ads},0}$. Lateral interactions are neglected in the calculation of γ_j as the NH_x coverages are low on the facets (see Figure 5c). As the NH_x surface species exhibit similar coverages on all facets (see Figure 5f), the average NH_x coverages are used in eq 1 for all facets.

Two Wulff-constructed NPs with sizes of about 4.3 nm (Ru₃₀₃₆ and Ru₂₉₅₈) are visualized in Figure 2c. The atop sites are colored according to the generalized coordination number (GCN).^{29,30} The left particle represents the NP in the first tank (reactor inlet), whereas the right particle shows the NP during the reaction conditions in the last tank (reactor outlet). The two structures clearly demonstrate that the presence of surface species significantly alters the NP shapes and modifies the distribution of GCN on the NP.

In PAKS-R, the shapes of the NPs are allowed to change in response to the reaction conditions. The scheme for the adaptive procedure is shown in the gray dashed rectangle in Figure 2d. The self-consistent shapes of the Wulff-constructed NPs are determined by an iterative loop between particle shape via the surface energies and the coverages. In the iterative loop, the coverages are initially calculated by kMC simulations based on the NP shapes in the absence of surface species (γ_j^0). The surface energies (γ_j) are updated with eq 1 using the calculated coverages. This process continues until convergence is achieved between the particle shape and coverages. For the present system, approximately five iterations are required for convergence. The self-consistent loop ensures that the reaction occurs over a particle with a Wulff shape in thermodynamic equilibrium with the reaction conditions. The iterative loop in the gray dashed rectangle is omitted for reactor simulations without NP shape changes.

The reaction kinetics are highly affected by the local reaction conditions, which are governed by the ongoing reaction and the mass transfers within the reactor.² In PAKS-R, the coupling between the local reaction conditions and the reaction kinetics is treated by using an on-the-fly iterative procedure. The flowchart with red rectangles in Figure 2d outlines the workflow for obtaining the kinetic properties over the reactor. In the PFR model, the partial pressures of gaseous species s (p_s^0) in tank 1 are given by the inlet partial pressures (p_s^{in}). From tank 2 to tank 10, the partial pressures of species s in tank $n + 1$ (p_s^{n+1}) are calculated by the kinetics and partial pressures in tank n (p_s^n) according to

$$p_s^{n+1} = p_s^n + \frac{RTm_n c_s \rho_{\text{site}} \overline{\text{TOF}}}{u} \quad (2)$$

where R [J/K = Pa m³/K] is the ideal gas constant. c_s is the stoichiometric coefficient of the gaseous species s . In the ammonia synthesis reaction, the stoichiometric coefficients of N₂, H₂, and NH₃ are -0.5 , -1.5 , and 1 , respectively. ρ_{site} [1/kg] is the number of surface sites per catalyst mass. u [m³/s] is the gas flow rate. As the change in gaseous molecule numbers in the reactor has a negligible effect on the flow rate, u is set to be constant. m_n [kg] is the mass of the catalysts in tank n , which is derived from the total catalyst mass m_{tot} in the reactor. Here, the values of ρ_{site} , u and m_{tot} are chosen to be consistent with the experiments in refs 10,21,22. In each tank of the reactor, the average TOF of the NP distribution ($\overline{\text{TOF}}$) is calculated by the total reaction rate divided by the total number of surface atoms, eq 3,

$$\overline{\text{TOF}} = \frac{\sum_i \text{TOF}_i \cdot \text{site}_i \cdot \text{number}_i}{\sum_i \text{site}_i \cdot \text{number}_i} \quad (3)$$

TOF_{*i*} is the TOF of particle i . site_{*i*} is the number of surface atoms on particle i . number_{*i*} is the number of i -particles in size distribution. The contribution of particle i to the total reaction rate (R_i) of particle i is defined by

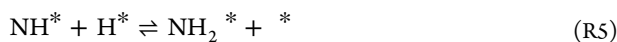
$$R_i = \text{TOF}_i \cdot \text{site}_i \cdot \text{number}_i \quad (4)$$

In PAKS-R, the majority of the computational costs are associated with the kMC simulations. The computational efficiency is enhanced by parallelization, where the kMC simulations of different NPs are performed on different computer cores (see Figure S1 for details).

DFT Calculations and kMC Simulations. The energy parameters in the DFT calculations are obtained using the BEEF-vdW exchange–correlation functional.³¹ All DFT calculations are carried out with the Vienna Ab initio Simulation Package (VASP)^{32–35} with the projector-augmented wave (PAW) scheme³⁶ to describe the interaction between the valence electrons and the core. The electronic states were expanded in a plane wave basis set with a 400 eV kinetic cutoff. To model the Ru NPs, the electronic energies are calculated for Ru(0001), Ru(10 $\bar{1}$ 0), Ru(10 $\bar{1}$ 1), Ru(10 $\bar{1}$ 2), and Ru(20 $\bar{2}$ 1), as well as models for step and edge sites. The reference energies of gaseous N₂, H₂, and NH₃ are optimized in a (10 × 10 × 10) Å³ box. All of the reaction energies in kMC simulations are zero-point corrected. Vibrational analysis is performed using the harmonic approximation with finite differences.

The ammonia synthesis reaction over metal catalysts is known to follow the dissociative reaction mechanism, where the first step is N₂ dissociation into atomic N, followed by sequential

hydrogenation of NH_x to gaseous NH_3 .³⁷ The seven elementary reaction steps (excluding diffusion events) considered are



Gaseous species are labeled with (g), and an asterisk represents a surface site. We included diffusion events for all surface species.

When NH_3 readsorption and dissociation are allowed during NH_3 synthesis, it is crucial that the reaction has the correct thermodynamic preference. The overall thermodynamics can be adjusted by modification of the stability of gaseous species.³⁸ In this work, we adjust the gaseous NH_3 energy by using the experimental reaction enthalpy of ammonia synthesis ($\Delta H = -0.48$ eV). After adjustment of the total NH_3 energy, the desorption energy of NH_3 (R7) decreases by 0.13 eV with respect to the unmodified DFT values, whereas the reaction energies and energy barriers for other elementary reactions remain unchanged.

The energy barriers for each reaction on all different types of sites on the Ru NPs are derived by linear scaling relations²⁷ as a function of the reaction energies (ΔE):

$$E_a = a\Delta E + b \quad (5)$$

The reaction energies are described by a scaling relation based on the generalized coordination number (GCN):^{29,30}

$$\Delta E = c \cdot \text{GCN} + d \quad (6)$$

The parameters a–d are fitted by DFT calculations on different surfaces. The GCN is defined as

$$\text{GCN}_i = \frac{1}{cn_{\max}} \sum_{j=1}^{n_i} cn_j \quad (7)$$

where n_i is the number of nearest neighbors of site i , cn_j is the coordination number of neighboring site j , and cn_{\max} is the maximum coordination number for atoms in hcp Ru bulk. All correlations between reaction energies and GCN have been reported in ref 27. Lateral interactions are important when describing the potential energy surface of the reaction. We include lateral interactions between all of the NH_x and H surface species. In addition, the dissociation barrier for N_2 has a dependence on adsorbed N atoms. The model for the lateral interactions is described in ref 27.

Supported metal NPs are inherently strained because of under-coordination and interaction with the support.³⁹ Following our recent work,²⁷ the inherent strain in the Ru NPs is modeled using the random normal distribution, eq 8,

$$f(\Delta s) = \frac{1}{\sigma\sqrt{2\pi}} \exp\left[-\frac{1}{2}\left(\frac{\Delta s - \mu}{\sigma}\right)^2\right] \quad (8)$$

where Δs is the strain on a site, μ is the mean value of strain, and σ is the standard deviation. Here, the values of μ and σ are set as

0 and 0.05, respectively. For Ru NPs, the changes in reaction energies and energy barriers induced by strain effects are added to the energy of each elementary reaction.²⁷

The adsorption of gaseous N_2 , H_2 , and NH_3 are considered to be barrierless, with the rate constants ($k_{s,n}^{\text{ads}}$) calculated according to collision theory:

$$k_{s,n}^{\text{ads}} = \frac{p_{s,n} A_{\text{site}}}{\sqrt{2\pi m k_B T}} \quad (9)$$

where $p_{s,n}$ is the partial gas pressure of gaseous species s in tank n . To ensure the thermodynamic consistency for reversible reactions, the rate constants for the desorption process are calculated via the equilibrium constant:

$$K_{s,n} = \frac{k_{s,n}^{\text{ads}}}{k_{s,n}^{\text{des}}} = \exp\left(-\frac{\Delta G^{\text{ads}}}{k_B T}\right) \approx \exp\left(-\frac{\Delta E^{\text{ads}} - T\Delta S^{\text{ads}}}{k_B T}\right) \quad (10)$$

where ΔG^{ads} , ΔE^{ads} , and ΔS^{ads} are the Gibbs free energy, adsorption energy, and adsorption entropy of the adsorption process, respectively. (The enthalpy is approximated with the electronic energy.) The rate constants for the elementary surface reactions are calculated using the harmonic transition state theory:

$$k = \kappa(T) \frac{k_B T}{h} \exp\left(-\frac{\Delta G_a}{k_B T}\right) \approx \kappa(T) \frac{k_B T}{h} \exp\left(-\frac{E_a - T\Delta S_a}{k_B T}\right) \quad (11)$$

where ΔG_a is the Gibbs free energy barrier, ΔS_a is the entropy barrier, and E_a is the energy barrier. $\kappa(T)$ is 1 for the NH_x hydrogenation reactions. For the N_2 dissociation step, $\kappa(T)$ is fitted to experiments^{40,41} to account for the low measured sticking probability.²⁷

The kMC simulations are carried out by using the MonteCoffee program,⁴² using coarse-grained adsorption sites. In this way, each coarse-grained entity contains hollow, bridge, and top positions, and the surface species are considered on the preferred geometric adsorption site. The reported TOF and coverages are obtained in the steady state. The coverages are calculated based on the normalized residence time.⁴³ The temperature is set to 673 K, and the partial pressures at the reactor inlet (tank 1) are 12.5 bar for N_2 , 37.5 bar for H_2 , and 0 bar for NH_3 , respectively. The settings in temperature and pressure are consistent with the experiments.^{10,21,22}

RESULTS AND DISCUSSION

Kinetics of Reactor Model. The conversion (X) and TOF ($\text{TOF}_{\text{reactor}}$) over the reactor are at stoichiometric conditions calculated with respect to the NH_3 partial pressure according to

$$X = \frac{p_{\text{NH}_3}^{\text{in}} - p_{\text{NH}_3}^{\text{out}}}{p_{\text{N}_2}^{\text{in}}} = \frac{2(p_{\text{NH}_3}^{\text{out}} - p_{\text{NH}_3}^{\text{in}})}{p_{\text{N}_2}^{\text{in}} + p_{\text{H}_2}^{\text{in}}} \quad (12)$$

$$\text{TOF}_{\text{reactor}} = \frac{(p_{\text{NH}_3}^{\text{out}} - p_{\text{NH}_3}^{\text{in}})u}{RTm_{\text{tot}} c_{\text{NH}_3} \rho_{\text{site}}} \quad (13)$$

where $p_{N_2}^{\text{in}}$, $p_{H_2}^{\text{in}}$, and $p_{NH_3}^{\text{in}}$ are the partial pressures of N_2 , H_2 , and NH_3 at the reactor inlet, respectively. $p_{NH_3}^{\text{out}}$ is the partial pressure of NH_3 at the reactor outlet.

Figure 3 shows the conversion and the TOF over the reactor for the distribution of particles as a function of the flow rate.

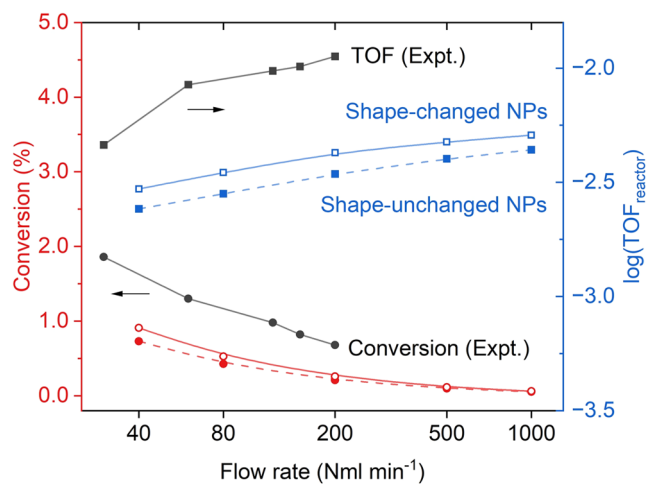


Figure 3. Conversion (red) and TOF_{reactor} (blue) versus flow rate. Temperature: 673 K. Partial pressures at reactor inlet: $p_{N_2} = 12.5$ bar, $p_{H_2} = 37.5$ bar, and $p_{NH_3} = 0$.

Experimentally measured^{10,21,22} conversion (black circles) and TOF_{reactor} (black squares) are indicated. Experimentally, X decreases from 1.9 to 0.7%, whereas the TOF_{reactor} increases from 4.6×10^{-3} to 1.1×10^{-2} $\text{site}^{-1} \text{s}^{-1}$ as the flow rate increases from 30 to 200 N mL min^{-1} . Computationally, the reactor model accounting for NP shape changes predicts a decrease of the X from 0.91 to 0.06%; simultaneously, the TOF_{reactor} increases from 2.96×10^{-3} to 5.09×10^{-3} $\text{site}^{-1} \text{s}^{-1}$, as the flow rate increases from 40 to 1000 N mL min^{-1} . The predicted X and TOF_{reactor} exhibit the same trends as the experimental observations. The differences in the values of both X and TOF_{reactor} are within a factor of 2, which falls within the expected margin of inherent error in the DFT calculations and the chosen particle distribution.

The X and TOF_{reactor} are determined by the reaction conditions and kinetics in each tank of the reactor model.

Figure 4a shows X as a function of tank number and catalyst mass. The contribution of tank n to conversion (X_n) is calculated according to

$$X_n = \frac{2(p_{NH_3}^n - p_{NH_3}^{n-1})}{p_{N_2}^{\text{in}} + p_{H_2}^{\text{in}}} = \frac{2RTm_n c_s \rho_{\text{site}} \overline{TOF}_n}{u(p_{N_2}^{\text{in}} + p_{H_2}^{\text{in}})} \quad (14)$$

where $p_{NH_3}^n$ and $p_{NH_3}^{n-1}$ are the NH_3 partial pressures in tank n and tank $n - 1$, respectively. As the conversion is low, we used the inlet pressures of N_2 and H_2 . \overline{TOF}_n is the average TOF of different NPs in tank n , which is calculated according to eq 3. The X_n reduces with the increasing flow rates because the higher flow rates increase the mass transfer and reduce the contact time between the catalysts and the reactant gas.

According to eq 14, X_n is determined by \overline{TOF}_n . Figure 4b shows the \overline{TOF}_n as a function of tank number or catalyst mass. \overline{TOF}_n decreases with increasing tank number, suggesting that the contribution of each unit catalyst mass to the overall reaction rate decreases along the reactor. In DFT-based kinetic models, some fixed reactant and product partial pressures are used to match the experimental operating conditions. In such an approach, the TOF calculated by the kinetic model is equal to the average TOF of some tanks in the reactor. Choosing the pressures for the reactor inlet (outlet) would result in a TOF that is higher (lower) than the $\overline{TOF}_{\text{reactor}}$, which is determined by integrating over all of the tanks in the reactor. Thus, it is important to have a full reactor model that accounts for the changes in the pressures along the reactor.

To assess the effect of NP shape changes on the reaction kinetics, we compare the X_n with and without NP-reshaping at a flow rate of 80 N mL min^{-1} , see Figure 4a. The results show that NP shape changes enhance the X at the reactor outlet by from 0.4 to 0.5%. To further explore how NP-reshaping affects the reaction kinetics at different positions of the reactor, Figure 4c presents the \overline{TOF}_n with and without NP-reshaping as a function of tank number or catalyst mass. Accounting for NP-reshaping in tank 1 has no effect on the kinetic properties, as the NP shapes remain close to unchanged under the chosen reaction conditions. From tank 2 to tank 10, the NP-reshaping leads to an increase in \overline{TOF}_n by about 20%.

Particle Resolved Activity. Knowing the kinetic properties of the reactor, we analyze the contribution of individual NP to

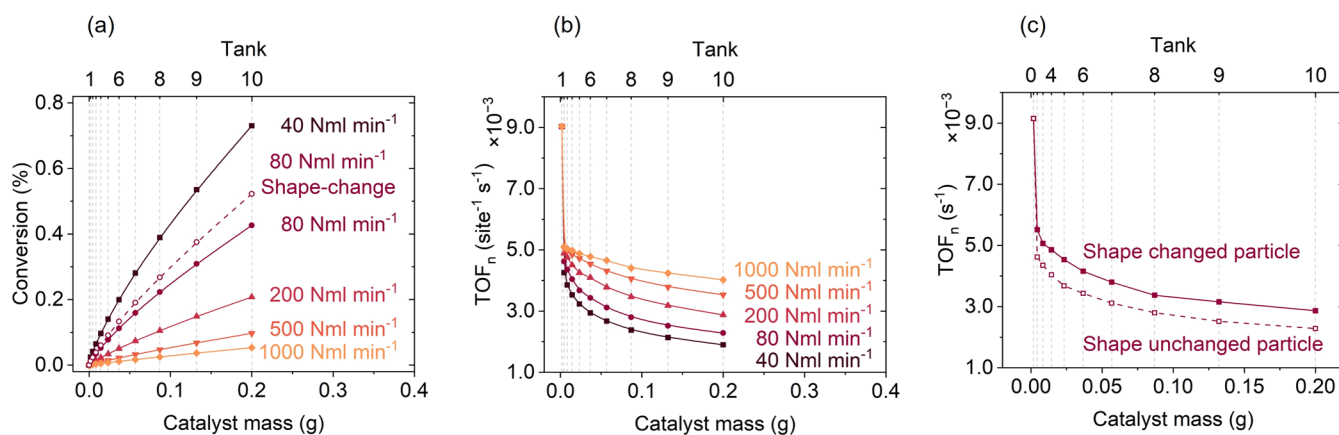


Figure 4. (a) Conversion, (b) \overline{TOF}_n at different flow rates, and (c) \overline{TOF}_n with and without NPs reshaping versus catalyst mass (tank number). Temperature: 673 K. Partial pressures at reactor inlet: $p_{N_2} = 12.5$ bar, $p_{H_2} = 37.5$ bar, and $p_{NH_3} = 0$. Flow rate in (c): 80 N mL min^{-1} .

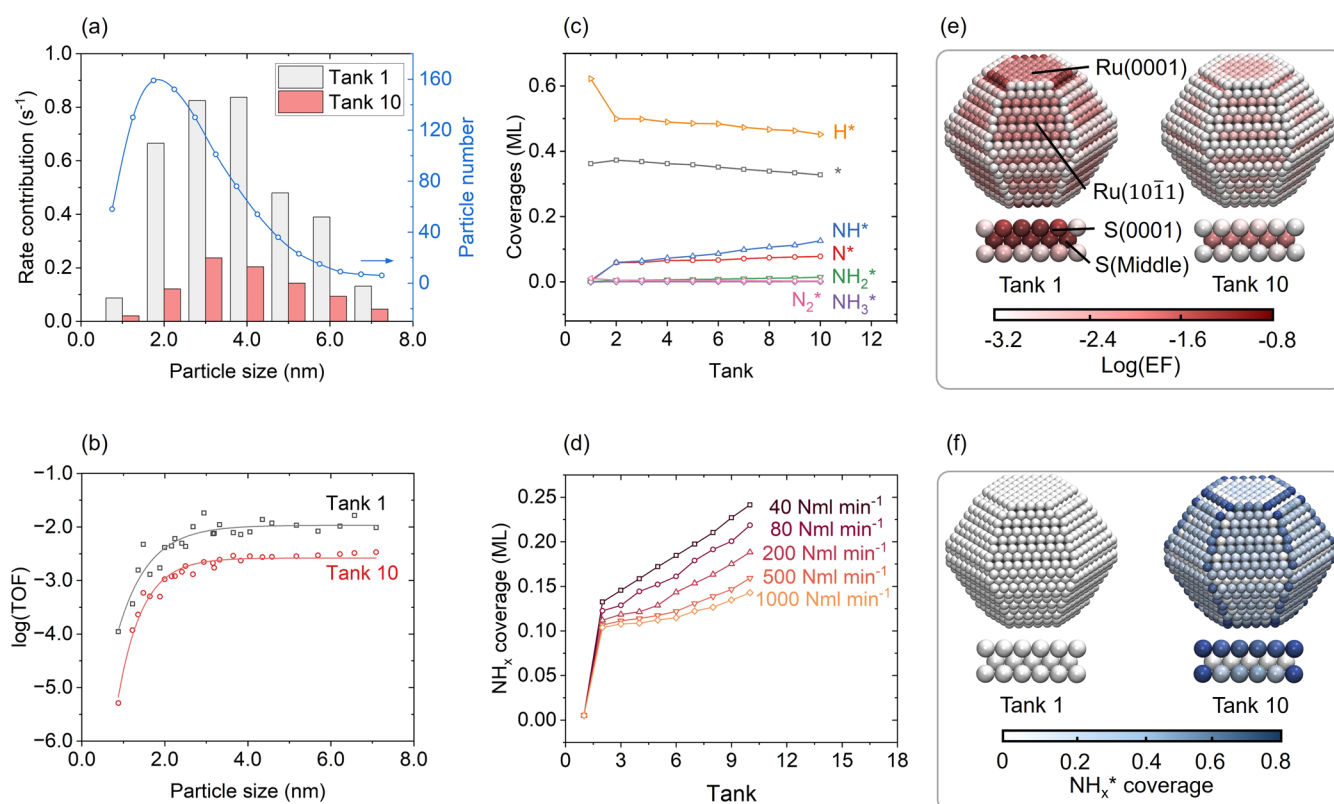


Figure 5. (a) Rate contributions (left) and particle number (right) versus particle size. (b) $\log(\text{TOF})$ versus particle size. (c) Averaged coverages on Ru₃₀₃₆ NP versus tank number. (d) Averaged NH_x coverages on Ru₃₀₃₆ NP at different flow rates versus tank number. (e) Event frequency (EF) for the N₂ dissociation step and (f) NH_x coverages on Ru₃₀₃₆ NP and A_s step sites. Temperature: 673 K. Partial pressures at reactor inlet: $p_{\text{N}_2} = 12.5$ bar, $p_{\text{H}_2} = 37.5$ bar, and $p_{\text{NH}_3} = 0$.

the reaction rate (R_i). Figure 5a shows the R_i in tank 1 (gray bar) and tank 10 (red bar) as a function of particle size ranging from 0.88 to 7.09 nm, along with the particle size distribution (blue curve). We consider, in total, 26 different particle sizes in each tank. The same number and distribution of particles are used in each tank. More than 65% of the Ru NP are below 2 nm in the experimental size distribution. However, according to our results, NPs smaller than 2 nm make minor contributions to the total reaction rate, accounting for 22 and 16% of the total rate in tanks 1 and 10, respectively. In contrast, although only 28% of the NPs are in the size range of 3.0–5.0 nm, this size range contributes more than 50% to the total reaction rate. The difference between the distributions of R_i and the particle number highlights that the small Ru NPs make a small contribution to the overall reaction rate.

The particle size-dependent kinetic properties are further analyzed by the TOF for different NPs, Figure 5b. The TOFs in tanks 1 and 10 exhibit similar trends, suggesting that the particle size-dependent TOF is not significantly affected by the reaction conditions. The TOF increases with particle size up to about 3 nm, beyond which it remains constant. For the ammonia synthesis reaction over Ru NPs, the rate-limiting N₂ dissociation step is facilitated by the presence of step sites with high GCN (GCN > 8).^{10,40,44} The lower TOF observed for small-sized Ru NPs is related to the lack of high-GCN sites. As the particle size exceeds 3 nm, high-GCN sites appear on the NPs, thereby enhancing the catalytic activity, which is consistent with experiments.²⁵ Considering the scarcity of Ru metal, the optimal size of Ru NPs for the ammonia synthesis reaction is suggested to be about 3 nm.

A Ru NP of 4.58 nm was selected (Ru₃₀₃₆) to investigate the details of the kinetics. Figure 5c shows the average coverages of each surface species for tanks 1 to 10. The coverages on the facets are generally lower than the coverage on the edges and corners. In tank 1, H atom is the dominant surface species with a coverage of about 0.6 monolayer (ML). From tank 2 to tank 10, the coverages of N atom and NH species increase, whereas the coverage of H atom decreases. In tank 10, N atom and NH species coverages are 0.08 and 0.13 ML, respectively, and the H atom coverage is 0.45 ML. The coverages of N₂, NH₂, and NH₃ species remain below 0.01 ML in all tanks due to their low adsorption energies. The coverages of NH_x species are in equilibrium with the chemical potential of gaseous NH₃ because each NH_x hydrogenation/dehydrogenation and NH₃ adsorption/desorption are much faster than the N₂ dissociation step. In tank 1, the absence of gaseous NH₃ at the reactor inlet leads to low coverages of the N atom and NH species. As the NH₃ partial pressure increases from tank 2 to tank 10, the N atom and NH coverages increase accordingly.

To explain the kinetic results that a higher flow rate leads to an increasing TOF_{reactor} in Figure 3, we show the average coverage of NH_x species at different flow rates in Figure 5d, which is calculated as the sum of average coverages of N atom, NH, NH₂, and NH₃ on Ru₃₀₃₆ NP. In the ammonia synthesis reaction, the rate of the N₂ dissociation step depends on the NH_x coverages via (i) reduction of the number of available free sites and (ii) increased barrier for dissociation.^{10,45} At higher flow rates, the buildup of an NH₃ partial pressure in the reactor decreases due to shorter contact time between the reactant and the catalyst, which leads to reduced NH_x coverages. The reduction in NH_x

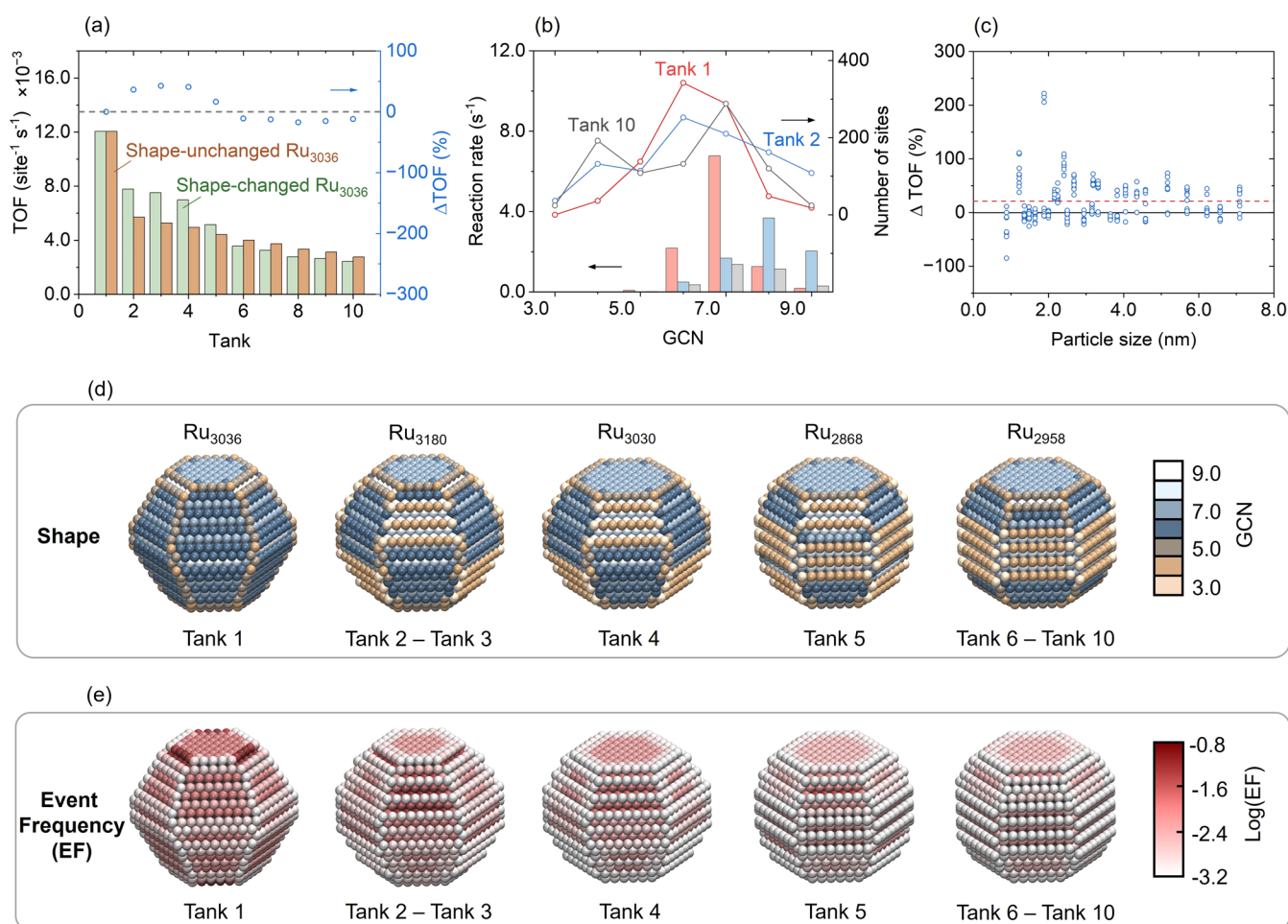


Figure 6. (a) TOF (left) and relative TOF difference, Δ TOF (right), with and without shape changes on Ru₃₀₃₆ NP versus tank number. (b) Reaction rate of the N₂ dissociation step (left) and the site number (right) on Ru₃₀₃₆ NP versus GCN. (c) Δ TOF versus particle size. (d) GCN and (e) event frequency (EF) for the N₂ dissociation step on Ru₃₀₃₆ NP from tank 1 to tank 10. Temperature: 673 K. Partial pressures at reactor inlet: p_{N_2} = 12.5 bar, p_{H_2} = 37.5 bar, and p_{NH_3} = 0.

coverages provides more free sites and weakens the impact of lateral interactions for the N₂ dissociation barrier, thereby enhancing the catalytic activity.

To explore the contribution of different sites on reaction rate, we plot a color map of TOF for the N₂ dissociation step on the Ru₃₀₃₆ NP, Figure 5e. The well-known B₃ step sites are absent on Ru₃₀₃₆ NP; however, the A₅ step sites with a similar local structure are present.⁴⁶ In tank 1, the A₅ step sites show a much higher TOF compared to other sites, owing to their lower activation barrier for the N₂ dissociation step. Specifically, on the A₅ step, the middle sites [S(middle)], with a GCN of 9.17, exhibit an event frequency (EF) of 0.15 site⁻¹ s⁻¹, whereas the S(0001) sites, with a GCN of 5.50, have an EF of 0.11 site⁻¹ s⁻¹. In tank 10, however, the EFs at the S(middle) and S(0001) sites reduce to 0.026 and 0.0045 site⁻¹ s⁻¹, respectively. The reduced TOF at the A₅ step sites suggests that the kinetics of active sites are highly sensitive to the NH₃ partial pressure.

To further understand how the changes in reaction conditions affect the kinetics, Figure 5f shows a color map of the NH_x coverage on the Ru₃₀₃₆ NP. In tank 1, the energy barrier of the N₂ dissociation step is not affected by the lateral interaction owing to the low coverage of N atoms. In tank 10, the increasing NH_x coverage significantly impacts the kinetics. On A₅ step sites, the NH_x coverage is about 0.8 ML on S(0001) sites but remains

nearly zero on S(middle) sites. As a result, the presence of NH_x species reduces the number of free sites available for the N₂ dissociation step on S(0001) sites and increases the energy barrier of the N₂ dissociation step on neighboring S(middle) sites through the lateral interaction with adsorbed N. The difference in H coverage across different tanks has a negligible effect on the kinetics because the H₂ partial pressure that determines the H coverage remains nearly unchanged along the reactor (Figure S2). Based on the analysis of A₅ step sites, the reduction of TOF in tank 10 can be related to the increased NH_x and N coverage, which decreases the rate of the N₂ dissociation step by reducing the number of available free sites and increasing the energy barrier.

Analysis of NPs Reshaping. The reaction conditions in the reactor affect the shapes of NP via the adsorbate-induced NP-reshaping.^{14,47} To illustrate how the shape changes influence the reaction kinetics, Figure 6a shows the TOF of Ru₃₀₃₆ NP with (TOF_{changed}) and without NPs reshaping (TOF_{unchanged}) across the 10 tanks. To quantify the effect in each tank, we calculate the relative TOF differences (Δ TOF):

$$\Delta\text{TOF} = \frac{\text{TOF}_{\text{changed}} - \text{TOF}_{\text{unchanged}}}{\text{TOF}_{\text{unchanged}}} \times 100\% \quad (15)$$

A positive (negative) value of Δ TOF indicates that the shape changes lead to an increase (decrease) in the TOF. In tank 2, the shape changes lead to an increased TOF, with a Δ TOF of 43%. From tank 2 to tank 5, the Δ TOF is about 20%. From tank 6 to tank 10, the shape changes reduce the TOF, with a Δ TOF value of about -10% . The changes in Δ TOF across the different tanks suggest that the impact of NP-reshaping on kinetics is highly sensitive to the reaction conditions.

To gain deeper insight into how shape changes affect the structures and the kinetics of Ru₃₀₃₆ NP, Figure 6b shows the distributions of GCN for the surface atoms in the particle (lines) and the reaction rate for N₂ dissociation (bars) for tanks 1, 2, and 10. Additionally, Figure 6d,e shows the color maps of GCN and EF for N₂ dissociation in all tanks. Note that the number of atoms in the Wulff-constructed NPs changes slightly with the shape to have the complete facets. The NP in tank 5 has 2868 atoms, whereas the NP in tank 2 has 3180 atoms. Given that the rate-limiting N₂ dissociation step is facilitated by high-GCN sites,^{10,40} we focus on changes in the number of high-GCN sites. In tank 1, there are 66 high-GCN (GCN > 8) sites on Ru₃₀₃₆ NP, dominated by A₅ step sites. In tank 2, the number of high-GCN sites on the NP increases to 270. The additional high-GCN sites are mainly located in the Ru(10 $\bar{1}$ 1) facet. The increasing number of high-GCN sites promotes N₂ dissociation and enhances the TOF. From tank 3 to tank 10, the shape changes of the NPs increase the ratio of Ru(10 $\bar{1}$ 0) and Ru(0001) facets, whereas the contribution of Ru(10 $\bar{1}$ 1) facets is reduced. The reduction in the Ru(10 $\bar{1}$ 1) facet decreases the number of high-GCN sites, which lowers the TOF.

Knowing the impact of shape changes on the Ru₃₀₃₆ NP, we extend our analysis to the 10 sets of the 26 NPs in the 10 tanks, Figure 6c. The distribution of Δ TOF exhibits a wide range, from -85 to 222% . Both positive and negative values appear in the distribution, indicating that the NP shape changes can either enhance or reduce the rate for the different NPs. Considering the averaged TOF over the reactor (Figure 4c), we find that the relative difference in TOF_{reactor} with and without NP-reshaping is about 20%, as indicated by the red dashed line in Figure 6c. This shows that the average effect of NP shape changes on the rate is smaller than that for the individual particles. Given that the Δ TOF values for individual NPs have a wide distribution, arbitrarily selecting a single NP for kinetic simulations would not necessarily capture the averaged kinetic properties of all NPs. Consequently, relying only on the computational results from a single NP may lead to an incomplete or even inaccurate understanding of the effect of NP shape changes.

Discussion of Computational Choices. The presented results are, of course, dependent on a range of computational choices. The kinetic parameters are obtained by using scaling relations, which are based on DFT calculations. We have used an exchange–correlation functional (vdW-BEEF)³¹ that is known to describe the surface kinetics properly.⁴⁸ As the applied reaction network allows for readsorption and dissociation of the product, it is crucial that the thermodynamics of the reaction is described properly. This is guaranteed by adjusting³⁸ the total energy of the gaseous NH₃.

The use of scaling relations enables kinetic simulations over NPs with a distribution of different types of sites. It is clear that scaling reduces kinetic differences that might exist between different sites; however, the importance of differences between sites is reduced during reaction conditions owing to adsorbate–adsorbate interactions and kinetic couplings.⁴⁹ The sensitivity of the results on the slopes of the scaling relations is, for the same

reason, low, which we have confirmed by explicit simulations with different slopes.²⁷

We have, in the current work, performed simulations for an ensemble of NPs using an experimentally measured size distribution¹⁰ of Wulff-shaped particles. The choice of using the Wulff-construction is a reasonable assumption, as detailed experimental knowledge on particle shapes is missing. The Wulff-construction is based on the calculated surface energies. The sensitivity of the NP shapes (and kinetic properties) to errors in the surface energies are, however, low as very large errors in the surface energies are required to obtain markedly different shapes. Quantum size effects could influence the properties of particles smaller than about 2 nm. However, only six of the 26 particles in the size distribution are below 2 nm, and the contribution to the activity from these particles is low because of the small amount of sites with GCN > 9.

Nanoparticles are inherently strained because of the large surface area and the interaction with the support. The choice in the present work was to use a random strain pattern with a standard deviation of 0.05, which is close to the value measured by high-precision scanning transmission electron microscopy for Pt NP being 0.03.³⁹ We have recently investigated these effects in detail for ammonia synthesis over Ru NP,²⁷ showing that increasing the standard deviation leads to a higher TOF. At low flow rates, a standard deviation of 0.1 could double the conversion.

CONCLUSIONS

The catalytic activity measured over technical catalysts is an average of the activity from a distribution of particle sizes and shapes. To allow for direct comparisons between experimental results and kinetic Monte Carlo (kMC) simulations, it is essential to consider the complexity of the technical catalyst under real reaction conditions.

Here, we develop a method—particle-shape adaptive kinetic Monte Carlo simulations in a reactor model (PAKS-R)—that provides a robust framework to directly compare Monte Carlo kinetics with the averaged catalytic activities observed over an experimental reactor. In PAKS-R, the kMC simulations are based on DFT calculations, and the shape of the considered particles changes as a response to the adsorbate coverages. A distribution of particle size is considered, and a reactor model is applied to account for changing gas composition because of the ongoing catalytic reaction. Through iterative processes between kMC simulations and reactor simulations, a self-consistent solution is obtained that can be compared with the averaged kinetic properties similar to what is measured over technical catalysts.

PAKS-R is used to model the ammonia synthesis reaction over a distribution of Ru NPs. The model successfully reproduces the experimental conversion and TOF over the reactor. We investigate the effect of flow rate and find that the TOF increases with increased flow rate. The enhanced TOF is a consequence of a reduced NH₃ partial pressure, which lowers the NH_x coverages and increases the number of free sites available for N₂ dissociation. We find that NP-reshaping can either enhance or reduce the TOF for individual NPs. Thus, neglecting the particle shape and size distributions may lead to an incomplete or even inaccurate understanding of the effect of NP shape changes. PAKS-R considers the kinetic properties for distributions of NPs and accounts for how the NPs respond to the reaction conditions. The method is general and will be useful

for reactions where the kinetics are sensitive to the particle sizes and shapes or to the reaction conditions.

■ ASSOCIATED CONTENT

SI Supporting Information

The Supporting Information is available free of charge at <https://pubs.acs.org/doi/10.1021/acscatal.5c01592>.

The considered 26 nanoparticles, description of the parallelization, and H coverage for the Ru₃₀₃₆ NP. (PDF)

■ AUTHOR INFORMATION

Corresponding Authors

Yuyi Yang – Department of Physics and Competence Centre for Catalysis, Chalmers University of Technology, SE-41296 Göteborg, Sweden; Email: yuyiy@chalmers.se

Anders Hellman – Department of Physics and Competence Centre for Catalysis, Chalmers University of Technology, SE-41296 Göteborg, Sweden; orcid.org/0000-0002-1821-159X; Email: ahell@chalmers.se

Henrik Grönbeck – Department of Physics and Competence Centre for Catalysis, Chalmers University of Technology, SE-41296 Göteborg, Sweden; orcid.org/0000-0002-8709-2889; Email: ghj@chalmers.se

Complete contact information is available at: <https://pubs.acs.org/doi/10.1021/acscatal.5c01592>

Notes

The authors declare no competing financial interest.

■ ACKNOWLEDGMENTS

Financial support by the Swedish Research Council (2024-05250) and Chalmers Area of Advance Nano is acknowledged. The calculations were performed at NSC via a NAISS grant (2024/3-26). The Competence Center for Catalysis (KCK) is hosted by Chalmers University of Technology and is financially supported by the Swedish Energy Agency and the member companies Johnson Matthey, Perstorp, Powercell, Preem, Scania CV, Umicore, and the Volvo Group.

■ REFERENCES

- (1) Hansen, P. L.; Wagner, J. B.; Helveg, S.; Rostrup-Nielsen, J. R.; Clausen, B. S.; Topsøe, H. Atom-resolved imaging of dynamic shape changes in supported copper nanocrystals. *Science* **2002**, *295*, 2053–2055.
- (2) Bruix, A.; Margraf, J. T.; Andersen, M.; Reuter, K. First-principles-based multiscale modelling of heterogeneous catalysis. *Nat. Catal.* **2019**, *2*, 659–670.
- (3) Ertl, G. Reactions at surfaces: from atoms to complexity (Nobel lecture). *Angew. Chem., Int. Ed.* **2008**, *47*, 3524–3535.
- (4) Somorjai, G. A.; Contreras, A. M.; Montano, M.; Rioux, R. M. Clusters, surfaces, and catalysis. *Proc. Natl. Acad. Sci. U.S.A.* **2006**, *103*, 10577–10583.
- (5) Henry, C. R. Surface studies of supported model catalysts. *Surf. Sci. Rep.* **1998**, *31*, 231–325.
- (6) Seh, Z. W.; Kibsgaard, J.; Dickens, C. F.; Chorkendorff, I.; Nørskov, J. K.; Jaramillo, T. F. Combining theory and experiment in electrocatalysis: Insights into materials design. *Science* **2017**, *355*, eaad4998.
- (7) Vogt, C.; Weckhuysen, B. M. The concept of active site in heterogeneous catalysis. *Nat. Rev. Chem.* **2022**, *6*, 89–111.
- (8) Saliccioli, M.; Stamatakis, M.; Caratzoulas, S.; Vlachos, D. G. A review of multiscale modeling of metal-catalyzed reactions: Mechanism development for complexity and emergent behavior. *Chem. Eng. Sci.* **2011**, *66*, 4319–4355.
- (9) Chen, B. W. J.; Xu, L.; Mavrikakis, M. Computational methods in heterogeneous catalysis. *Chem. Rev.* **2021**, *121*, 1007–1048.
- (10) Honkala, K.; Hellman, A.; Remediakis, I.; Logadottir, A.; Carlsson, A.; Dahl, S.; Christensen, C. H.; Nørskov, J. K. Ammonia synthesis from first-principles calculations. *Science* **2005**, *307*, 555–558.
- (11) Nørskov, J. K.; Bligaard, T.; Rossmeisl, J.; Christensen, C. H. Towards the computational design of solid catalysts. *Nat. Chem.* **2009**, *1*, 37–46.
- (12) Jørgensen, M.; Grönbeck, H. The site-assembly determines catalytic activity of nanoparticles. *Angew. Chem., Int. Ed.* **2018**, *57*, 5086–5089.
- (13) Vojvodic, A.; Medford, A. J.; Studt, F.; Abild-Pedersen, F.; Khan, T. S.; Bligaard, T.; Nørskov, J. Exploring the limits: A low-pressure, low-temperature Haber-Bosch process. *Chem. Phys. Lett.* **2014**, *598*, 108–112.
- (14) Zhu, B.; Meng, J.; Yuan, W.; Zhang, X.; Yang, H.; Wang, Y.; Gao, Y. Reshaping of metal nanoparticles under reaction conditions. *Angew. Chem., Int. Ed.* **2020**, *59*, 2171–2180.
- (15) Shi, X.; Lin, X.; Luo, R.; Wu, S.; Li, L.; Zhao, Z.-J.; Gong, J. Dynamics of heterogeneous catalytic processes at operando conditions. *JACS Au* **2021**, *1*, 2100–2120.
- (16) Smil, V. Detonator of the population explosion. *Nature* **1999**, *400*, 415.
- (17) Service, R. F. Liquid sunshine. *Science* **2018**, *361*, 120–123.
- (18) Erisman, J. W.; Sutton, M. A.; Galloway, J.; Klimont, Z.; Winiwarter, W. How a century of ammonia synthesis changed the world. *Nat. Geosci.* **2008**, *1*, 636–639.
- (19) Jacobsen, C. J. H.; Dahl, S.; Clausen, B. S.; Bahn, S.; Logadottir, A.; Nørskov, J. K. Catalyst design by interpolation in the periodic table: bimetallic ammonia synthesis catalysts. *J. Am. Chem. Soc.* **2001**, *123*, 8404–8405.
- (20) Boisen, A.; Dahl, S.; Nørskov, J. K.; Christensen, C. H. Why the optimal ammonia synthesis catalyst is not the optimal ammonia decomposition catalyst. *J. Catal.* **2005**, *230*, 309–312.
- (21) Dahl, S.; Sehested, J.; Jacobsen, C.; Törnqvist, E.; Chorkendorff, I. Surface science based microkinetic analysis of ammonia synthesis over ruthenium catalysts. *J. Catal.* **2000**, *192*, 391–399.
- (22) Hellman, A.; Honkala, K.; Remediakis, I.; Logadottir, A.; Carlsson, A.; Dahl, S.; Christensen, C. H.; Nørskov, J. K. Ammonia synthesis and decomposition on a Ru-based catalyst modeled by first-principles. *Surf. Sci.* **2009**, *603*, 1731–1739.
- (23) Fang, H.; Liu, D.; Luo, Y.; Zhou, Y.; Liang, S.; Wang, X.; Lin, B.; Jiang, L. Challenges and opportunities of Ru-based catalysts toward the synthesis and utilization of ammonia. *ACS Catal.* **2022**, *12*, 3938–3954.
- (24) Jacobsen, C. J.; Dahl, S.; Hansen, P. L.; Törnqvist, E.; Jensen, L.; Topsøe, H.; Prip, D. V.; Møenshaug, P. B.; Chorkendorff, I. Structure sensitivity of supported ruthenium catalysts for ammonia synthesis. *J. Mol. Catal. A* **2000**, *163*, 19–26.
- (25) Raróg-Pilecka, W.; Miśkiewicz, E.; Szmigiel, D.; Kowalczyk, Z. Structure sensitivity of ammonia synthesis over promoted ruthenium catalysts supported on graphitised carbon. *J. Catal.* **2005**, *231*, 11–19.
- (26) Rahm, J. M.; Erhart, P. WulffPack: A Python package for Wulff constructions. *J. Open Source Software* **2020**, *5*, 1944.
- (27) Yang, Y.; Hellman, A.; Grönbeck, H. Inherent strain and kinetic coupling determine the kinetics of ammonia synthesis over Ru nanoparticles. *Nat. Commun.* **2025**, *16*, No. 1625.
- (28) Duan, M.; Yu, J.; Meng, J.; Zhu, B.; Wang, Y.; Gao, Y. Reconstruction of supported metal nanoparticles in reaction conditions. *Angew. Chem.* **2018**, *130*, 6574–6579.
- (29) Calle-Vallejo, F.; Martínez, J. L.; García-Lastra, J. M.; Sautet, P.; Loffreda, D. Fast prediction of adsorption properties for platinum nanocatalysts with generalized coordination numbers. *Angew. Chem., Int. Ed.* **2014**, *53*, 8316–8319.
- (30) Calle-Vallejo, F.; Loffreda, D.; Koper, M. T.; Sautet, P. Introducing structural sensitivity into adsorption–energy scaling relations by means of coordination numbers. *Nat. Chem.* **2015**, *7*, 403–410.
- (31) Wellendorff, J.; Lundgaard, K. T.; Møgelhøj, A.; Petzold, V.; Landis, D. D.; Nørskov, J. K.; Bligaard, T.; Jacobsen, K. W. Exchange-

correlation model development with Bayesian error estimation. *Phys. Rev. B* **2012**, *85*, 235149.

(32) Kresse, G.; Furthmüller, J. Efficient iterative schemes for ab initio total-energy calculations using a plane-wave basis set. *Phys. Rev. B* **1996**, *54*, 11169.

(33) Kresse, G.; Furthmüller, J. Efficiency of ab-initio total energy calculations for metals and semiconductors using a plane-wave basis set. *Comput. Mater. Sci.* **1996**, *6*, 15–50.

(34) Kresse, G.; Hafner, J. Ab initio molecular dynamics for liquid metals. *Phys. Rev. B* **1993**, *47*, 558.

(35) Kresse, G.; Joubert, D. From ultrasoft pseudopotentials to the projector augmented-wave method. *Phys. Rev. B* **1999**, *59*, 1758.

(36) Blöchl, P. E. Projector augmented-wave method. *Phys. Rev. B* **1994**, *50*, 17953.

(37) Ertl, G. Surface science and catalysis-studies on the mechanism of ammonia synthesis: the PH Emmett award address. *Catal. Rev.* **1980**, *21*, 201–223.

(38) Studt, F.; Abild-Pedersen, F.; Varley, J. B.; Nørskov, J. K. CO and CO₂ hydrogenation to methanol calculated using the BEEF-vdW functional. *Catal. Lett.* **2013**, *143*, 71–73.

(39) Pingel, T. N.; Jørgensen, M.; Yankovich, A. B.; Grönbeck, H.; Olsson, E. Influence of atomic site-specific strain on catalytic activity of supported nanoparticles. *Nat. Commun.* **2018**, *9*, No. 2722.

(40) Dahl, S.; Logadóttir, A.; Egeberg, R.; Larsen, J.; Chorkendorff, I.; Törnqvist, E.; Nørskov, J. K. Role of steps in N₂ activation on Ru(0001). *Phys. Rev. Lett.* **1999**, *83*, 1814.

(41) Logadóttir, A.; Nørskov, J. K. Ammonia synthesis over a Ru(0001) surface studied by density functional calculations. *J. Catal.* **2003**, *220*, 273–279.

(42) Jørgensen, M.; Grönbeck, H. MonteCoffee: A programmable kinetic Monte Carlo framework. *J. Chem. Phys.* **2018**, *149*, No. 114101, DOI: 10.1063/1.5046635.

(43) Andersen, M.; Panosetti, C.; Reuter, K. A practical guide to surface kinetic Monte Carlo simulations. *Front. Chem.* **2019**, *7*, 202.

(44) Goodwin, C. M.; Lömker, P.; Degerman, D.; Davies, B.; Shipilin, M.; Garcia-Martinez, F.; Koroidov, S.; Katja Mathiesen, J.; Rameshan, R.; Rodrigues, G. L.; et al. Operando probing of the surface chemistry during the Haber-Bosch process. *Nature* **2024**, *625*, 282–286.

(45) Mhadeshwar, A.; Kitchin, J.; Barteau, M.; Vlachos, D. The role of adsorbate-adsorbate interactions in the rate controlling step and the most abundant reaction intermediate of NH₃ decomposition on Ru. *Catal. Lett.* **2004**, *96*, 13–22.

(46) Casey-Stevens, C. A.; Lambie, S. G.; Ruffman, C.; Skulason, E.; Garden, A. L. Geometric and electronic effects contributing to N₂ dissociation barriers on a range of active sites on Ru nanoparticles. *J. Phys. Chem. C* **2019**, *123*, 30458–30466.

(47) Svensson, R.; Grönbeck, H. Dynamics of Dilute Nanoalloy Catalysts. *J. Phys. Chem. Lett.* **2024**, *15*, 7885–7891.

(48) Medford, A. J.; Wellendorff, J.; Vojvodic, A.; Studt, F.; Abild-Pedersen, F.; Jacobsen, K. W.; Bligaard, T.; Nørskov, J. K. Assessing the reliability of calculated catalytic ammonia synthesis rates. *Science* **2014**, *345*, 197–200.

(49) Jørgensen, M.; Grönbeck, H. Perspectives on Computational Catalysis for Metal Nanoparticles. *ACS Catal.* **2019**, *9*, 8872–8881.